The Astrophysical Journal Letters, 789:L31 (6pp), 2014 July 10 doi:10.1088/2041-8205/789/2/L31

DISCOVERY OF A STRONG LENSING GALAXY EMBEDDED IN A CLUSTER AT $z = 1.62$*

Kenneth C. Wong[1,9], Kim-Vy H. Tran[2], Sherry H. Suyu[1], Ivelina G. Momcheva[3], Gabriel B. Brammer[4], Mark Brodwin[5], Anthony H. Gonzalez[6], Aleksi Halkola, Glenn G. Kacprzak[7,10], Anton M. Koekemoer[4], Casey J. Papovich[2], and Gregory H. Rudnick[8]

[1] Institute of Astronomy and Astrophysics, Academia Sinica (ASIAA), P.O. Box 23-141, Taipei 10617, Taiwan
[2] George P. and Cynthia W. Mitchell Institute for Fundamental Physics and Astronomy, Department of Physics and Astronomy, Texas A&M University, College Station, TX 77843, USA
[3] Astronomy Department, Yale University, New Haven, CT 06511, USA
[4] Space Telescope Science Institute, 3700 San Martin Drive, Baltimore, MD 21218, USA
[5] Department of Physics and Astronomy, University of Missouri, 5110 Rockhill Road, Kansas City, MO 64110, USA
[6] Department of Astronomy, University of Florida, Gainesville, FL 32611, USA
[7] Swinburne University of Technology, Victoria 3122, Australia
[8] Department of Physics and Astronomy, The University of Kansas, Malott Room 1082, 1251 Wescoe Hall Drive, Lawrence, KS 66045, USA
Received 2014 May 12; accepted 2014 June 10; published 2014 June 23

ABSTRACT

We identify a strong lensing galaxy in the cluster IRC 0218 (also known as XMM-LSS J02182−05102) that is spectroscopically confirmed to be at $z = 1.62$, making it the highest-redshift strong lens galaxy known. The lens is one of the two brightest cluster galaxies and lenses a background source galaxy into an arc and a counterimage. With *Hubble Space Telescope* (*HST*) grism and Keck/LRIS spectroscopy, we measure the source redshift to be $z_S = 2.26$. Using *HST* imaging in ACS/F475W, ACS/F814W, WFC3/F125W, and WFC3/F160W, we model the lens mass distribution with an elliptical power-law profile and account for the effects of the cluster halo and nearby galaxies. The Einstein radius is $\theta_E = 0.38^{+0.02}_{-0.01}$ arcsec ($3.2^{+0.2}_{-0.1}$ kpc) and the total enclosed mass is $M_{tot}(<\theta_E) = 1.8^{+0.2}_{-0.1} \times 10^{11}\,M_\odot$. We estimate that the cluster environment contributes ∼10% of this total mass. Assuming a Chabrier initial mass function (IMF), the dark matter fraction within θ_E is $f_{DM}^{Chab} = 0.3^{+0.1}_{-0.3}$, while a Salpeter IMF is marginally inconsistent with the enclosed mass ($f_{DM}^{Salp} = -0.3^{+0.2}_{-0.5}$). The total magnification of the source is $\mu_{tot} = 2.1^{+0.4}_{-0.3}$. The source has at least one bright compact region offset from the source center. Emission from Lyα and [O III] are likely to probe different regions in the source.

Key words: galaxies: clusters: individual (XMM-LSS J02182–05102) – galaxies: elliptical and lenticular, cD – galaxies: structure – gravitational lensing: strong

Online-only material: color figures

1. INTRODUCTION

Gravitational lensing is a powerful tool for studying the mass structure of galaxies. Lensing studies of early-type galaxies (ETGs) at $z < 1$ have produced interesting results on their properties. Their total mass density profile slope γ' (where $\rho(r) \propto r^{-\gamma'}$) depends solely on the surface stellar mass density at fixed redshift, whereas γ' of individual galaxies does not evolve significantly (Koopmans et al. 2006; Barnabè et al. 2013; Sonnenfeld et al. 2013). ETGs also favor a heavier stellar initial mass function (IMF; Auger et al. 2010; Sonnenfeld et al. 2012). Nonetheless, the evolution of the mass distribution of ETGs at $z > 1$ is not well constrained. Identifying strong lensing galaxies at $z > 1$ provides leverage on how ETGs assemble and tests the current cosmological paradigm.

However, strong lensing galaxies are increasingly rare at higher redshifts due to the evolving galaxy mass function, decreasing background volume, and decreasing lensing efficiency. Distant lenses also require high-resolution imaging to separate the source and lensing galaxy, and near-infrared spectroscopy to confirm their redshifts. van der Wel et al. (2013) reported the most distant strong lensing galaxy known thus far at $z_L = 1.53$ and estimated one $z_L > 1$ system per ∼200 arcmin^2.

Here, we report the discovery of a strong lensing galaxy embedded in a cluster at $z = 1.62$ (Papovich et al. 2010; Tanaka et al. 2010), making it the highest-redshift strong lens galaxy known (in contrast with the highest-redshift strong lens cluster at $z = 1.75$; Gonzalez et al. 2012). The system is unusual because of the high lens redshift, and the lens being the most massive cluster member. The system lies in the Ultra-Deep Survey (UDS) legacy field, which has extensive multi-wavelength observations (Lawrence et al. 2007; Galametz et al. 2013; Skelton et al. 2014). Spectroscopy taken with the *Hubble Space Telescope* (*HST*) grisms and the Low Resolution Imaging Spectrometer (LRIS; Oke et al. 1995) on Keck confirm the source redshift of $z_S = 2.26$. We combine the data sets to model the lens, including its environment. We assume $\Omega_m = 0.3$, $\Omega_\Lambda = 0.7$, and $H_0 = 70\,\mathrm{km\,s^{-1}\,Mpc^{-1}}$. All quantities are in h_{70} units. At $z = 1.62$, the angular scale is $1'' = 8.47$ kpc. We use AB magnitudes.

2. OBSERVATIONS

2.1. Keck/LRIS Spectroscopy

Using the Keck/LRIS, we carried out a spectroscopic survey of the cluster IRC 0218 on 2012 October 19 and 20 (NASA/Keck Program ID 48/2012B). Targets were selected

* Based on observations made with the NASA/ESA *Hubble Space Telescope*, obtained at the Space Telescope Science Institute, which is operated by the Association of Universities for Research in Astronomy, Inc., under NASA contract NAS 5-26555. These observations are associated with program No. 12590.
[9] EACOA Fellow.
[10] Australian Research Council Super Science Fellow.

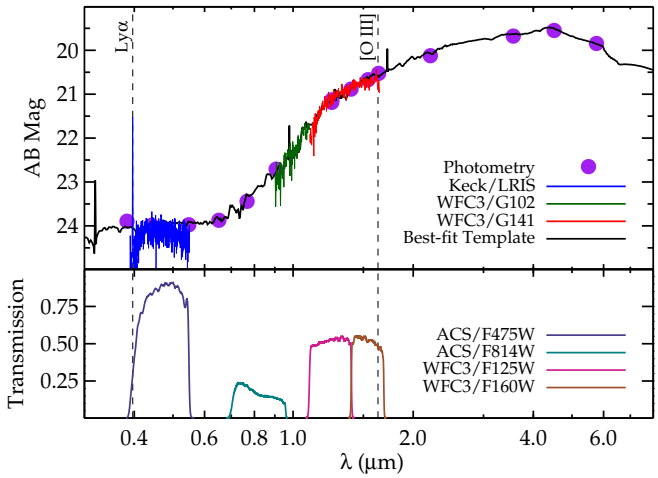

Figure 1. Top: total fluxes for the lens system as measured by 3D-HST (object 31684; Skelton et al. 2014) that combines ground-based imaging with *HST* and *Spitzer* observations (purple). The best-fit spectral energy distribution from EAZY is included (black). Also shown are the blended Keck/LRIS spectrum (blue) and the *HST*/WFC3 G102 (green) and G141 (red) grism spectra for the lens. The spectra are arbitrarily normalized for clarity. The grism spectra trace the lens galaxy's Balmer break at $z_L = 1.64$. The spectra show strong Lyα and [O III] $\lambda\lambda$4959, 5007 emission from the source at $z_S = 2.26$. Bottom: filter transmission curves for the *HST* imaging used in the lens modeling. A bright point source corresponding to emission at $z_S = 2.26$ is visible in the ACS/F475 (Lyα) and WFC3/F160 ([O III] $\lambda\lambda$4959, 5007) images.

(A color version of this figure is available in the online journal.)

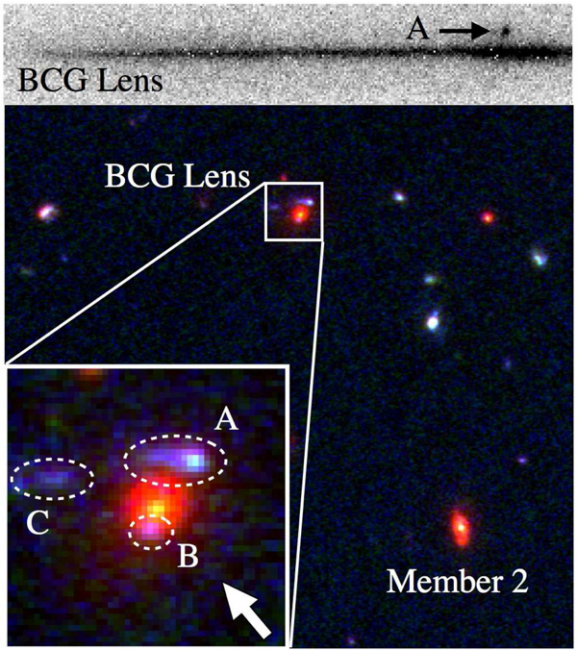

Figure 2. Top: negative image of the *HST* WFC3/G141 grism spectrum for the lensing galaxy (continuum). Approximately ∼0.″5 above the lens is [O III] $\lambda\lambda$4959, 5007 emission from object A at $z_S = 2.26$. Bottom: false-color image of the UDS cluster core generated with *HST* imaging (ACS/F475W, ACS/F814W, WFC3/F125W, and WFC3/F160W). North and east are up and left, respectively. Labeled are the BCG lens and the other BCG (Member 2). The inset ($3'' \times 3''$) shows the lens with the arc (A) and counterimage (B) labeled. Another faint galaxy (C) is weakly detected by the grism and consistent with $z \sim 2.26$. The arrow indicates the dispersion direction of the grism observations (top).

(A color version of this figure is available in the online journal.)

from the Williams et al. (2009) catalog of the UDS taken as part of the UKIRT Infrared Deep Sky Survey (Lawrence et al. 2007). The *K*-selected catalogs reach 5σ-limiting magnitudes in 1.″75 diameter apertures of $B < 27.7$, $R < 27.1$, $i < 26.8$, $z < 25.5$, $J < 23.9$, and $K < 23.6$.

We use the 600/4000 grism for the blue side and the 600/10000 grating for the red side of LRIS. With 1″ slit widths, the resolutions are 4.0 Å and 4.7 Å, respectively. Observing conditions were excellent with ∼0.″6 median seeing. The total integration time on the lens is 9 hr. We reduce the spectra following Tran et al. (2007), using IRAF[11] routines with custom software provided by D. Kelson (Kelson 2003). The wavelength coverage of the extracted spectra is 3800–5800 Å (blue side) and 7000–10000 Å (red side). A full analysis of this redshift survey will be presented in K.-V. H. Tran et al. (in preparation).

We use XCSAO (Kurtz et al. 1992) with various templates for Lyman-break and Lyα emitting galaxies from Shapley et al. (2003) to measure a redshift for the blended spectrum composed of the lens galaxy and the lensed source. The strong emission detected at 3957 Å (Figure 1, top) has the asymmetric profile characteristic of Lyα (Shapley et al. 2003) and corresponds to a redshift of $z_S = 2.25384 \pm 0.00003$. The observed Ly$\alpha$ equivalent width (EW), derived for a continuum fit between 1180–1250 Å rest frame, is 129.4 ± 4.6 Å.

2.2. HST Observations

The UDS cluster falls in a legacy field that has extensive multi-wavelength observations, including deep *HST* imaging from CANDELS (0.″06 pixel^{-1}; Grogin et al. 2011; Koekemoer et al. 2011) and G141 spectroscopy from 3D-HST (Brammer et al. 2012). Additional *HST* imaging and G102 spectroscopy were obtained in GO-12590 (PI: C. Papovich). Figure 1 shows the total fluxes measured for the more massive of the two brightest cluster galaxies (BCGs) from the 3D-HST catalog of the UDS field (Skelton et al. 2014), which includes *Spitzer*/IRAC. Hereafter, the BCG refers to this more massive galaxy unless otherwise stated. The BCG shows excess flux at $\lambda < 5000$ Å due to emission from the lensed source. At longer wavelengths, the lens galaxy dominates. Grism spectroscopy confirms the BCG redshift of $z_L = 1.6406^{+0.0018}_{-0.0050}$. We attribute the redshift difference between the BCG and cluster to peculiar velocities due to the unrelaxed nature of the cluster (e.g., Martel et al. 2014), consistent with the high fraction of star-forming members (Tran et al. 2010). We use $z = 1.62$ as the lens redshift for cosmological calculations.

The lens and source are blended in ground-based observations, but *HST*'s resolution (Figure 2) separates the system into the BCG, an arc (object A), and a counterimage (object B). In the grism spectra, the BCG shows strong continuum. Approximately 0.″5 above the BCG in the G141 spectrum is a compact emission line corresponding to [O III] $\lambda\lambda$4959, 5007 at $z_S = 2.2623 \pm 0.0002$ from object A. We also detect [O III] $\lambda\lambda$4959, 5007 corresponding to object B once we remove the lens galaxy's light (I. G. Momcheva et al. in preparation). The faint object C shows weak [O III] $\lambda\lambda$4959, 5007 in the grism spectrum consistent with a redshift of $z_S = 2.26$.

3. MODELING THE STRONG LENSING SYSTEM

Combining our ground-based spectroscopy and *HST* observations, we confirm that the strong lensing system is composed

[11] IRAF is distributed by the National Optical Astronomy Observatory, which is operated by the Association of Universities for Research in Astronomy, Inc., under cooperative agreement with the National Science Foundation.

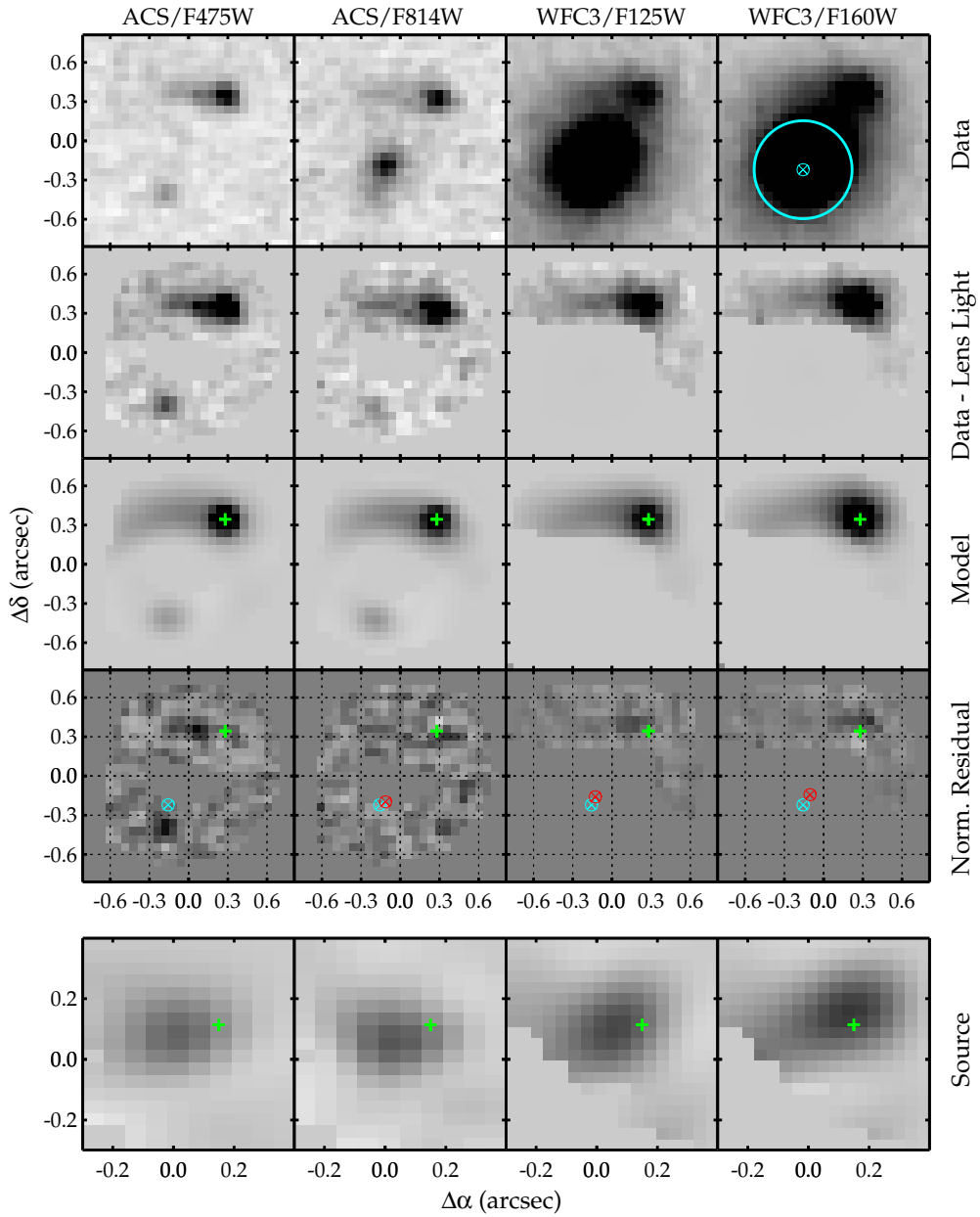

Figure 3. Top row: negative *HST* images of the strong lensing system in the ACS/F475W, ACS/F814W, WFC3/F125W, and WFC3/F160W filters. The images are 1.″62 on a side. The cyan cross denotes the centroid of the mass distribution, and the cyan circle the Einstein radius. Second row: images with the lens light subtracted. Only the pixels containing the lensed source are shown and used in the lens modeling. Third row: reconstructed image plane from the best-fit lens model. The model includes a compact emission region (point source convolved with the PSF) marked by the green cross. Fourth row: normalized image plane residuals where the color scale shows the $\pm 2\sigma$ range. The green cross denotes the position of the compact source as in the third row. The magnification varies by ~0.5 over the region around the compact source. Grid lines are overplotted for clarity. The centroid of the lens light distribution in each filter (red cross) is offset from that of the mass (cyan cross). Bottom row: extended source reconstruction. The compact emission region is not reconstructed since it is unresolved, but its inferred location from the lens model is indicated (green cross). The source morphology is less constrained in the F125W and F160W because only the upper half-annulus is used in the model. The compact emission is offset from the source galaxy's center in all filters.

(A color version of this figure is available in the online journal.)

of the BCG lens and source. We model the system with Glee, a software developed by S. H. Suyu and A. Halkola (Suyu & Halkola 2010; Suyu et al. 2012). Lensing mass distributions are parameterized profiles, and background sources are modeled on a pixel grid (Suyu et al. 2006). The lens galaxy light distributions are modeled as Sérsic profiles. Unresolved point sources on the pixel grid are modeled as point images on the image plane. Model parameters of the lens and the source are constrained through Markov Chain Monte Carlo (MCMC) sampling.

3.1. Lens Model

Taking a 27 × 27 pixel region around the lens, we utilize the deepest *HST* images spanning the widest wavelength range: ACS/F475W, ACS/F814W, WFC3/F125W, and WFC3/F160W (Figure 3, top rows). We model the lens galaxy as an elliptical singular power-law mass distribution with the mass profile slope parameterized as $\Gamma = (\gamma' - 1)/2$ (where the three-dimensional mass density is $\rho(r) \propto r^{-\gamma'}$). We adopt a

uniform prior of $0.2 \leqslant \Gamma \leqslant 0.8$. The projected axis ratio b/a has a uniform prior ($0.3 \leqslant b/a \leqslant 1$) with the position angle as a free parameter. The normalization of the mass profile is set by the Einstein radius $\theta_{\rm E}$, which is also a free parameter. We adopt a Gaussian prior on the mass centroid with a width of $\sigma = 0\farcs05$ (see Koopmans et al. 2006) that is centered on the fitted light centroid of the lens galaxy in the WFC3/F160W image ($\lambda_{\rm rest} \sim 0.6\,\mu$m).

We first remove the lens galaxy's light using a single Sérsic profile, as this is sufficient to describe the lens light in the region of the lensed images. In F814W, we exclude the annular region containing the lensed images (objects A and B; Figure 2) when fitting the lens light profile. Because the lens is considerably brighter than the counterimage (object B; Figure 2) in F125W and F160W, we exclude only the half-annulus around arc A when fitting the lens light profile.

To constrain the lens mass parameters, we use image pixels in the annular regions in F475W and F814W and the half-annular regions in F125W and F160W (Figure 3, second row) that contain the lensed images. We construct weight images for each filter by adding Poisson noise from sources to the inverse variance images, as outlined in Koekemoer et al. (2011) for CANDELS. Glee simultaneously models across the four bands and reconstructs the source onto a grid of 20×20 pixels with a resolution of $\sim 0\farcs05$. Our lens model also requires a point source convolved with the point-spread function (PSF) coincident with the peak surface brightness in image A (Figure 2). The position of this point source is the same across all filters and fit simultaneously with the lens model parameters. The counterimage of the point source is not modeled separately given its low magnification.

3.2. Modeling Lens Environment Contributions

The lens galaxy is embedded in a cluster, and the overdense environment may affect the lens model (e.g., Momcheva et al. 2006; Wong et al. 2011). We model cluster galaxies within $2'$ of the lens as singular isothermal spheres truncated at r_{200} and estimate their virial masses assuming the stellar-to-halo mass relation of Moster et al. (2013). We parameterize the cluster's dark matter halo as a spherical Navarro–Frenk–White (NFW) profile (Navarro et al. 1996) with a mass of $7.7 \times 10^{13}\,M_\odot$ centered at the peak of the X-ray emission (source 12A in Pierre et al. 2012) and a concentration calculated using the mass–concentration relation of Zhao et al. (2009).

In addition to this fiducial model, we run an extensive suite of models to test environmental contributions to the lens. We explore multiple permutations with and without: (1) nearby cluster galaxies; (2) the cluster dark matter halo; (3) additional external shear; (4) galaxies along the line of sight, assumed to be in the lens plane. We also run test models that allow the cluster halo centroid to vary by the $25''$ uncertainty on the X-ray emission centroid (Pierre et al. 2012), as well as models where we double the cluster mass.

In exploring this wide variety of models, we find that they provide fits of comparable quality, and the inferred parameters (e.g., θ_E) among the different models agree to within their statistical uncertainties. We adopt our fiducial power-law ellipsoid lens model with a fixed NFW halo for the cluster and fixed isothermal halos for the cluster galaxies because it is realistic and has the fewest additional free parameters.

4. RESULTS

4.1. Properties of the Lensing Galaxy

With our fiducial lens model, we measure an Einstein radius of $\theta_{\rm E} = 0.38^{+0.02}_{-0.01}$ arcsec ($3.2^{+0.2}_{-0.1}$ kpc) and total mass enclosed within $\theta_{\rm E}$ of $1.8^{+0.2}_{-0.1} \times 10^{11}\,M_\odot$. From our environment model, we estimate that the cluster halo and other cluster members contribute $\sim$10% of this enclosed mass ($\sim$7% and $\sim$3%, respectively), consistent with results at $z \lesssim 0.5$ (Treu et al. 2009). Increasing the environment contribution would increase this fraction (e.g., a cluster halo with double the mass would contribute $\sim$15% of the enclosed mass), but θ_E remains robust to within the model uncertainties. The lens galaxy's mass within $\theta_{\rm E}$ is thus $\sim 1.6 \times 10^{11}\,M_\odot$.

Following Papovich et al. (2012), we now model the lens light in F160W with a two-component model using an $n = 4$ bulge and $n = 1$ disk. The arc is masked, although the source flux is negligible compared to the lens flux (<3%). Papovich et al. (2012) measure the total stellar mass assuming a Chabrier (2003) IMF with solar metallicity. We integrate the light profile and calculate the stellar mass within $\theta_{\rm E}$ to be $1.3^{+0.5}_{-0.2} \times 10^{11}\,M_\odot$, corresponding to a dark matter fraction of $f_{\rm DM}^{\rm Chab}(<\theta_{\rm E}) = 0.3^{+0.1}_{-0.3}$. If we use a Salpeter (1955) IMF, which seems to be preferred for ETGs at $z < 1$ (e.g., Auger et al. 2010; Cappellari et al. 2012; Sonnenfeld et al. 2012; Conroy et al. 2013), the enclosed stellar mass is $2.2^{+0.9}_{-0.4} \times 10^{11}\,M_\odot$ and is larger than the enclosed total mass ($f_{\rm DM}^{\rm Salp}(<\theta_{\rm E}) = -0.3^{+0.2}_{-0.5}$), albeit at marginal significance. This is an upper limit on the dark matter fraction of the galaxy, as the environment contributes $\sim$10% of the total mass within $\theta_{\rm E}$.

In the three reddest filters (the lens is undetected in F475W), the centroids of the lens light profile and of the mass model are offset by as much as $\sim$1.5 pixels ($\sim 0\farcs1$; Figure 3). Studies of $z \lesssim 0.5$ ETGs do not find significant offsets between their mass and light (Koopmans et al. 2006). However, the lens light centroid shifts among different bands, suggesting that the youngest stars are displaced from the older population. The different stellar populations may not all directly trace the dark matter.

4.2. Properties of the Lensed Source

The source is magnified by a factor of $2.1^{+0.4}_{-0.3}$. The unlensed source has an extended profile with a bright compact region that is mapped to the outskirts of the source (Figure 3). We fit a Sérsic profile to the extended source to measure its flux. To compute the total flux (Table 1), we add the flux from the compact emission, which is determined by taking the flux of the fitted PSF component and dividing by the magnification at that location ($|\mu_A|$ in Table 1). We estimate the modeling uncertainty to be $\sim$0.15 mag by fitting to a subset of sources reconstructed from samples in the MCMC chain. Combined with the photometric uncertainties, the total uncertainty is $\sim$0.2 mag. The effective radius varies between $r_{\rm eff} \sim 0\farcs11$–$0\farcs20$.

There is residual image flux (Figure 3, fourth row) that we attribute to compact emission regions in the source. The residuals shift in both intensity and position among the bands, likely because of different emission lines (Figure 1, bottom): F814W samples only the continuum and has the smallest residuals, while F475W has Lyα and F160W has [O III] $\lambda\lambda$4959, 5007 emission. Indeed, Lyα emission can be spatially offset from continuum emission in galaxies at $z > 2$ (e.g., Feldmeier et al. 2013; Momose et al. 2014). We speculate that offset [O II] λ3727

Table 1
Observed Quantitiesand Lens Model Parameters

Parameter	Value
Observed quantities	
α, δ (J2000)	02:18:21.5, −05:10:19.9
$z_{\rm L}$ (grism)	$1.6406^{+0.0018}_{-0.0050}$
$z_{\rm S}$ (grism)	2.2623 ± 0.0002
$z_{\rm S}$ (Lyα)	2.25384 ± 0.00003
Lyα EW$_{\rm observed}$(Å)	129.4 ± 4.6
WFC3/F125W (mag)[a]	21.19 ± 0.01
WFC3/F160W (mag)[a]	20.67 ± 0.01
$M_\star^{\rm Chab}$ (10^{11} $M_\odot$)[b]	$2.0^{+0.8}_{-0.3}$
$M_\star^{\rm Salp}$ (10^{11} $M_\odot$)[b]	$3.5^{+1.4}_{-0.6}$
Bulge + Disk profile (F160W)	
Bulge ($n = 4$) $r_{\rm eff}$ ($''$)	$0.15^{+0.04}_{-0.03}$
Disk ($n = 1$) $r_{\rm eff}$ ($''$)	$0.72^{+0.10}_{-0.07}$
Lens model: Galaxy parameters[c]	
$\mu_{\rm tot}$	$2.1^{+0.4}_{-0.3}$
$\lvert\mu_A\rvert$[d]	$1.8^{+0.3}_{-0.2}$
$\lvert\mu_B\rvert$[d]	$0.3^{+0.1}_{-0.1}$
Δx ($''$)[e]	$-0.05^{+0.01}_{-0.02}$
Δy ($''$)[e]	$-0.08^{+0.02}_{-0.02}$
$\theta_{\rm E}$ ($''$)	$0.38^{+0.02}_{-0.01}$
b/a	$0.8^{+0.1}_{-0.2}$
θ(°)	8^{+45}_{-41}
Γ	$0.70^{+0.06}_{-0.07}$
$M_{\rm tot}(<\theta_{\rm E})$ (10^{11} $M_\odot$)	$1.8^{+0.2}_{-0.1}$
$M_\star^{\rm Chab}(<\theta_{\rm E})$ (10^{11} $M_\odot$)	$1.3^{+0.5}_{-0.2}$
$M_\star^{\rm Salp}(<\theta_{\rm E})$ (10^{11} $M_\odot$)	$2.2^{+0.9}_{-0.4}$
$f_{\rm DM}^{\rm Chab}(<\theta_{\rm E})$	$0.3^{+0.1}_{-0.3}$
$f_{\rm DM}^{\rm Salp}(<\theta_{\rm E})$	$-0.3^{+0.2}_{-0.5}$
Reconstructed source: intrinsic values[c]	
ACS/F475W (mag)	25.5 ± 0.2
ACS/F814W (mag)	25.5 ± 0.2
WFC3/F125W (mag)	25.9 ± 0.2
WFC3/F160W (mag)	25.2 ± 0.2

Notes.
[a] Total magnitudes from Skelton et al. (2014).
[b] Total stellar masses from Papovich et al. (2012).
[c] For lens model quantities, the reported values are medians, with errors corresponding to the 16th and 84th percentiles.
[d] μ_A, μ_B are magnifications at the peak locations of the brighter and fainter images, respectively.
[e] Offset of mass profile centroid relative to galaxy light centroid in F160W.

emission may be causing the weaker residual feature in F125W. Although the G141 spectrum does not show it, [O II] λ3727 would fall in a region where the grism response is dropping, making this interpretation uncertain. These residuals cannot come from the same source position, as lensing is achromatic. The lens model uses the same position of the compact emission region (green cross, Figure 3) across the multiple bands, but because they are offset, the model compromises by placing the PSF between the peak fluxes. This results in residuals in all bands, even F814W where there is only continuum.

The largest residual is in F475W and is due to Lyα emission that is observed in both the arc and counterimage (objects A and B in Figure 2; see also Figure 3, left). To test if the bright Lyα emission is problematic for the lens modeling, we fit an additional PSF to the counterimage in F475W and subtract it a priori. Using only the upper half-annulus to model the lens, we find that the image residuals, inferred lens model parameters, and modeled source fluxes are nearly identical to that of our fiducial model.

The residuals corresponding to the emission-line regions extend in the direction of the arc (object A), i.e., tangential to the lens galaxy. This implies that the emission-line regions are elongated and/or stretched due to lensing.

5. CONCLUSIONS

We report the discovery of the highest-redshift strong lensing galaxy known to date. The unusual gravitational lens is the most massive member of the galaxy cluster IRC 0218 at $z = 1.62$. We measure spectroscopic redshifts for the lens and source of $z_{\rm L} = 1.6406^{+0.0018}_{-0.0050}$ and $z_{\rm S} = 2.2623 \pm 0.0002$, respectively. Only with *HST*'s resolution are we able to separate the lensing BCG from the source, which is multiply imaged into a bright arc and a counterimage. The source shows strong Lyα emission with an observed EW of 129.4 ± 4.6 Å as measured with Keck/LRIS.

We adopt a lens model that combines a power-law ellipsoid for the lens galaxy with an environmental component (fixed cluster NFW halo + isothermal halos for cluster galaxies). The Einstein radius is $\theta_{\rm E} = 0.38^{+0.02}_{-0.01}$ arcsec ($3.2^{+0.2}_{-0.1}$ kpc) and the total enclosed mass is $M_{\rm tot}(<\theta_{\rm E}) = 1.8^{+0.2}_{-0.1} \times 10^{11}\ M_\odot$. We estimate that the cluster environment contributes ∼10% of this total mass. Assuming a Chabrier IMF for the lens galaxy, the enclosed stellar mass is $M_\star(<\theta_{\rm E}) = 1.3^{+0.5}_{-0.2} \times 10^{11}\ M_\odot$ and the upper limit on the galaxy dark matter fraction is $f_{\rm DM}^{\rm Chab}(<\theta_{\rm E}) = 0.3^{+0.1}_{-0.3}$. Alternatively, a Salpeter IMF is marginally inconsistent with the enclosed mass, $f_{\rm DM}^{\rm Salp}(<\theta_{\rm E}) = -0.3^{+0.2}_{-0.5}$.

The reconstructed source has bright compact regions offset from the galaxy's center. These could be emission-line regions corresponding to Lyα and [O III] λλ4959, 5007 that likely probe different regions in the source.

Strong lensing galaxies at $z > 1$ directly measure the stellar build-up of massive galaxies (e.g., whether the IMF evolves with redshift), and their number tests the current cosmological paradigm. Ongoing and upcoming deep imaging surveys should identify more lensing candidates to directly study the dark matter and light distributions of structures when the universe was ∼30% of its current age.

We thank Chuck Keeton and Curtis McCully for helpful discussions. K.C.W. is supported by an EACOA Fellowship awarded by the East Asia Core Observatories Association, which consists of the Academia Sinica Institute of Astronomy and Astrophysics, the National Astronomical Observatory of Japan, the National Astronomical Observatory of China, and the Korea Astronomy and Space Science Institute. This work was supported by a NASA Keck Award, administered by the NExScI, and data presented were obtained at the W. M. Keck Observatory from telescope time allocated to NASA through the partnership with the California Institute of Technology and the University of California. The observatory was made possible by the generous financial support of the W. M. Keck Foundation. The authors recognize and acknowledge the very significant cultural role and reverence that the summit of Mauna Kea has always had within the indigenous Hawaiian community. This work is based on observations taken with the NASA/ESA *HST* by the 3D-HST

Treasury Program (GO 12177 and 12328), as well as by program GO 12590, supported by a NASA through a grant from the Space Telescope Science Institute. *HST* and STScI are operated by the Association of Universities for Research in Astronomy, Inc., under NASA contract NAS5-26555.

REFERENCES

Auger, M. W., Treu, T., Gavazzi, R., et al. 2010, ApJL, 721, L163
Barnabè, M., Spiniello, C., Koopmans, L. V. E., et al. 2013, MNRAS, 436, 253
Brammer, G. B., Sánchez-Janssen, R., Labbé, I., et al. 2012, ApJL, 758, L17
Cappellari, M., McDermid, R. M., Alatalo, K., et al. 2012, Natur, 484, 485
Chabrier, G. 2003, PASP, 115, 763
Conroy, C., Dutton, A. A., Graves, G. J., Mendel, J. T., & van Dokkum, P. G. 2013, ApJL, 776, L26
Feldmeier, J. J., Hagen, A., Ciardullo, R., et al. 2013, ApJ, 776, 75
Galametz, A., Grazian, A., Fontana, A., et al. 2013, ApJS, 206, 10
Gonzalez, A. H., Stanford, S. A., Brodwin, M., et al. 2012, ApJ, 753, 163
Grogin, N. A., Kocevski, Dale D., Faber, S. M., et al. 2011, ApJS, 197, 35
Kelson, D. D. 2003, PASP, 115, 688
Koekemoer, A. M., Faber, S. M., Ferguson, H. C., et al. 2011, ApJS, 197, 36
Koopmans, L. V. E., Treu, T., Bolton, A. S., Burles, S., & Moustakas, L. A. 2006, ApJ, 649, 599
Kurtz, M. J., Mink, D. J., Wyatt, W. F., et al. 1992, in ASP Conf. Ser. 25, Astronomical Data Analysis Software and Systems I, ed. D. M. Worrall, C. Biemesderfer, & J. Barnes (San Francisco, CA: ASP), 432
Lawrence, A., Warren, S. J., Almaini, O., et al. 2007, MNRAS, 379, 1599
Martel, H., Robichaud, F., & Barai, P. 2014, ApJ, 786, 79
Momcheva, I., Williams, K., Keeton, C., & Zabludoff, A. 2006, ApJ, 641, 169
Momose, R., Ouchi, M., Nakajima, K., et al. 2014, MNRAS, 442, 110
Moster, B. P., Naab, T., & White, S. D. M. 2013, MNRAS, 428, 3121
Navarro, J. F., Frenk, C. S., & White, S. D. M. 1996, ApJ, 462, 563
Oke, J. B., Cohen, J. G., Carr, M., et al. 1995, PASP, 107, 375
Papovich, C., Bassett, R., Lotz, J. M., et al. 2012, ApJ, 750, 93
Papovich, C., Momcheva, I., Willmer, C. N. A., et al. 2010, ApJ, 716, 1503
Pierre, M., Clerc, N., Maughan, B., et al. 2012, A&A, 540, A4
Salpeter, E. E. 1955, ApJ, 121, 161
Shapley, A. E., Steidel, C. C., Pettini, M., & Adelberger, K. L. 2003, ApJ, 588, 65
Skelton, R. E., Whitaker, K. E., Momcheva, I. G., et al. 2014, ApJS, submitted (arXiv:1403.3689)
Sonnenfeld, A., Treu, T., Gavazzi, R., et al. 2012, ApJ, 752, 163
Sonnenfeld, A., Treu, T., Gavazzi, R., et al. 2013, ApJ, 777, 98
Suyu, S. H., & Halkola, A. 2010, A&A, 524, A94
Suyu, S. H., Hensel, S. W., McKean, J. P., et al. 2012, ApJ, 750, 10
Suyu, S. H., Marshall, P. J., Hobson, M. P., & Blandford, R. D. 2006, MNRAS, 371, 983
Tanaka, M., Finoguenov, A., & Ueda, Y. 2010, ApJL, 716, L152
Tran, K.-V. H., Franx, M., Illingworth, G. D., et al. 2007, ApJ, 661, 750
Tran, K.-V. H., Papovich, C., Saintonge, A., et al. 2010, ApJL, 719, L126
Treu, T., Gavazzi, R., Gorecki, A., et al. 2009, ApJ, 690, 670
van der Wel, A., van de Ven, G., Maseda, M., et al. 2013, ApJL, 777, L17
Williams, R. J., Quadri, R. F., Franx, M., van Dokkum, P., & Labbé, I. 2009, ApJ, 691, 1879
Wong, K. C., Keeton, C. R., Williams, K. A., Momcheva, I. G., & Zabludoff, A. I. 2011, ApJ, 726, 84
Zhao, D. H., Jing, Y. P., Mo, H. J., & Börner, G. 2009, ApJ, 707, 354